



HAL
open science

TIME DEPENDENT SCANNING PATH OPTIMIZATION FOR THE POWDER BED FUSION ADDITIVE MANUFACTURING PROCESS

Mathilde Boissier, G Allaire, Christophe Tournier

► **To cite this version:**

Mathilde Boissier, G Allaire, Christophe Tournier. TIME DEPENDENT SCANNING PATH OPTIMIZATION FOR THE POWDER BED FUSION ADDITIVE MANUFACTURING PROCESS. Computer-Aided Design, 2022, 142, pp.103122. 10.1016/j.cad.2021.103122 . hal-03202102v2

HAL Id: hal-03202102

<https://hal.science/hal-03202102v2>

Submitted on 24 May 2021

HAL is a multi-disciplinary open access archive for the deposit and dissemination of scientific research documents, whether they are published or not. The documents may come from teaching and research institutions in France or abroad, or from public or private research centers.

L'archive ouverte pluridisciplinaire **HAL**, est destinée au dépôt et à la diffusion de documents scientifiques de niveau recherche, publiés ou non, émanant des établissements d'enseignement et de recherche français ou étrangers, des laboratoires publics ou privés.

TIME DEPENDENT SCANNING PATH OPTIMIZATION FOR THE POWDER BED FUSION ADDITIVE MANUFACTURING PROCESS

M. BOISSIER^{1,2*}, G. ALLAIRE¹, C. TOURNIER²

¹ CMAP, École Polytechnique, CNRS UMR7641, Institut Polytechnique de Paris, Palaiseau, France

² Université Paris-Saclay, ENS Paris-Saclay, LURPA, 91190 Gif-sur-Yvette, France

*mathilde.boissier@polytechnique.edu

Abstract: In this paper, scanning paths optimization for the powder bed fusion additive manufacturing process is investigated. The path design is a key factor of the manufacturing time and for the control of residual stresses arising during the building, since it directly impacts the temperature distribution. In the literature, the scanning paths proposed are mainly based on existing patterns, the relevance of which is not related to the part to build. In this work, we propose an optimization algorithm to determine the scanning path without a priori restrictions. Taking into account the time dependence of the source, the manufacturing time is minimized under two constraints: melting the required structure and avoiding any over-heating causing thermally induced residual stresses. The results illustrate how crucial the part's shape and topology is in the path quality and point out promising leads to define path and part design constraints.

Keywords. Path planning and control, additive manufacturing, metallic powder bed fusion, adjoint-based optimization

CONTENTS

1	Introduction	1
2	Modelling and optimization problem	2
2.1	Two dimensional thermal model	3
2.2	Optimization problem	3
3	Discrete model and optimization algorithm	4
3.1	Path representation and discrete model	4
3.2	Differentiation of the discrete optimization problem with respect to the discrete path	5
3.3	Transformation of the derivatives into gradients	8
3.4	Optimization algorithm	8
4	Numerical results	9
4.1	Aluminium test case	10
4.2	Titanium test case	15
5	Conclusion and perspectives	20
6	Acknowledgments	21

Highlights

- First systematic use of geometric sensitivity approach for path optimization
- Optimization under realistic partial differential equation constraint
- Numerical tests for real materials with calibrated physical parameters

1 Introduction

Powder bed fusion additive manufacturing consists in building an object layer by layer using metallic powder [7, 19, 29, 38]. For each layer, some powder is spread on top of the already built part and a heat source travels along a prescribed path to melt prescribed zones. This technology is very promising because of several advantages [26, 46]: better optimized and more complex parts can now be built because the manufacturing constraints are less demanding than in traditional technologies, mass production is not required anymore to make the process economically efficient which is very interesting in prototyping and repairing issues. However, such a building process complicates the control of the part's final quality. Indeed, the high temperatures involved cause several mechanical, metallurgical and thermal phenomena. Among the different defects to

mitigate (porosity, residual stresses, loss of alloy elements, anisotropy, surface roughness [19, 38, 42]), we especially focus here on residual stresses: mainly provoked by an ill-controlled temperature distribution, they can result in distortions, weaknesses or even cracks [37].

If several parameters are involved in the manufacturing process, the scanning path is one of the most important ones. Indeed, it directly impacts both the manufacturing time [27, 44] and the temperature distribution which governs the part's quality [20, 22, 30, 35, 42, 45]. The literature on scanning paths goes back to traditional machining (welding, milling [6, 17, 33, 43]), most of the works being based upon patterns or a priori fixed strategies [31]. Raster lines, contours, Medial Axis Transformation, fractals, etc.: in each case, the strategy is fixed independently from the part to build and the path adapted through few parameters optimization. If some works consider splitting into cells the area to melt, then matching them with scanning strategies [1, 30, 40], the optimization only focuses on these cells and the matching without considering any further scanning path modifications. Recently, three works proposed a different approach in which the path is fully optimized without any a priori restrictions. The work initiated by [34] in which the path is optimized for anisotropy has recently been extended to the control of residual stresses in [15]. The authors propose the optimization of a level set function corresponding to the scanning path. The defects are characterized by an inherent strain method under a steady state modelling assumption. A second work considers the scanning path optimization using optimal control [2, 3]. Theoretical results on the existence and uniqueness of solutions have been obtained in a transient context. Finally, in a third work [10], we optimize the scanning path in the steady state context by using shape optimization tools. There, the residual stresses are controlled through a temperature constraint. This method has then been extended to a concurrent optimization of the path and the part's shape and topology [11].

In the present paper we extend our previous approach of path optimization to the more realistic transient case, still controlling the residual stresses through the temperature. In [10], the path was represented as a broken line in which the distance between two consecutive points was fixed: the discrete path was determined by the sequence of angles between each element and the horizontal line, by the starting point and by the number of elements modelling the time required to travel along the path. This representation is not efficient because it makes the issue of scanning time minimization very complex [9]. A novel discretization is proposed in this work. The path is still represented by a broken line however defined directly by its nodal points: the length between two consecutive points is not fixed anymore. If this increases the computational costs of the process' simulation, this makes the notion of scanning time more intuitive. In line with the conclusions given in [11], the various numerical test cases, including some with different parts to build, show the efficiency of our approach and its ability to give a better understanding on how the path is related to the part's shape and topology.

Section 2 details the modelling choices made in this paper. Because of the number and complexity of the phenomena involved in the powder bed fusion manufacturing process, a macroscopic approach is chosen in which the powder and the solid only are considered. Then, the scanning path being defined on the layer plane, this model is made two dimensional. In the end, the optimization problem is defined as follows: the scanning time is minimized under the constraints of the correct melting of the part to build and the absence of over heating. The constraints are expressed as functions of the temperature only, avoiding any mechanical problem resolution including residual stresses computation.

Section 3 is concerned with algorithmic issues. First, a discretization of the optimization problem is proposed: the temperature is computed on a fixed mesh while the path is described by a broken line the nodal points of which must be optimized. Then, this problem is differentiated and, using an Augmented Lagrangian method to deal with the constraints, a descent direction is defined. Finally, the effective algorithm is detailed.

Section 4 presents the numerical results. The algorithm is tested for the building of three different parts and for two different materials (aluminium and titanium alloys). These various results provide information on the algorithm efficiency as well as intuition on the notion of optimal path and on how it is related to the part to build.

2 Modelling and optimization problem

Simulating the several complex phenomena involved in powder bed fusion processes (energy absorption, fluid mechanics of the melting pool for example) constitutes a research topic in its own [19, 38, 42] aimed at proposing and discussing compromises between accuracy and computational time. Two main categories spring up [25, 36]: the first one, referred to as "microscopic", is a high fidelity model implying a complete physical description of the process whereas the second one, called "macroscopic", relies on many simplifications thus proving to be much more economical in terms of computational costs. In this work, because the path is optimized using an iterative algorithm, several simulations are required which prohibits a microscopic approach. We present in this section the macroscopic model chosen and the resulting optimization problem. For further details on this model, the interested reader is referred to [9] and especially to Chapter 5.

2.1 Two dimensional thermal model

The macroscopic approach, involving only powder and solid, provides the control of the manufacturing time and the thermo-mechanical effects, especially thermal expansion and residual stresses. This latter requires plasticity models which hard resolution is frequently avoided in optimization (see [5, 8, 15] for alternate approaches). In this work, we choose to focus on the thermal problem only, assuming that these residual stresses are mainly caused by spatial temperature gradient and thermal expansion [19, 37]. Hence, on the contrary to the inherent strain method proposed in [15], we do not include any mechanical computation. On the other hand, we keep the problem's time dependence. Focusing on the temperature only is obviously a huge approximation but offers a relevant first step in setting path optimization algorithms and opens perspectives in considering a full thermo-mechanical system.

The focus is in this work on a single layer and thus on a two dimensional problem: the working or computational domain $\Sigma \subset \mathbb{R}^2$ corresponds to the top layer under building. At the initial time 0, the domain Σ is maintained at a fixed temperature y_{ini} . A source q is switched on, moved along a path Γ belonging to this layer until being switched off at the final time t_F . We focus on conduction effects only [48, 49] and, assuming that the considered layer is surrounded by low-conductive powder (compared to the solid's conductivity), adiabatic boundary conditions (Neumann) are chosen. The material coefficients such as the density ρ , the heat capacity c_p and the conduction λ are assumed to be independent from temperature, time and space (and thus fixed real numbers). The resulting heat equation given by (1) is finally a classic conduction heat equation to which has been added a correcting term $\beta(y - y_{ini})$ modelling the conduction in the building direction e_z (Figure 1) [9, 10].

$$\begin{cases} \rho c_p \partial_t y(t, x) - \nabla \cdot (\lambda \nabla y(t, x)) + \beta(y(t, x) - y_{ini}) = q(t, x) & \text{in } (0, t_F) \times \Sigma \\ \lambda \partial_n y(t, x) = 0 & \text{on } (0, t_F) \times \partial \Sigma \\ y(0, x) = y_{ini}(x) & \text{in } \Sigma. \end{cases} \quad (1)$$

The source is modeled as a Gaussian beam [19, 36] given by (2), with $\bar{P} > 0$ the source power, A an absorption coefficient, L a characteristic length related to the dimension loss and r related to the beam focus:

$$q(t, x) = \frac{A\bar{P}}{\pi L r^2} \exp\left(-\frac{|x - u(t)|^2}{r^2}\right) \quad 0 \leq t \leq t_F. \quad (2)$$

In the following, this notation is simplified introducing $P = \frac{A\bar{P}}{\pi L r^2}$. The source center $u(t)$ following the path Γ is solution of the trajectory ordinary differential equation, with V the (scalar) source speed and τ_Γ the tangent to the path:

$$\begin{cases} \dot{u}(t) = V(t)\tau_\Gamma(t) & t \in (0, t_F) \\ u(0) = u_0. \end{cases}$$

In this work, the velocity is kept constant $V = 1 \text{ms}^{-1}$. This model being the result of several assumptions, its coefficients have been calibrated and especially the coefficient β and the characteristic length L introduced because of the dimension loss. Further details on this calibration process can be found in [9] and the corresponding values chosen for the numerical applications are given in Section 4.

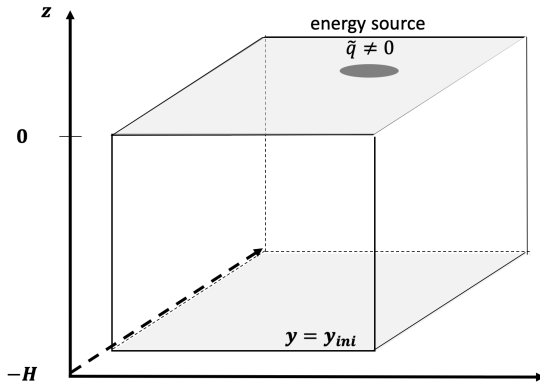


Figure 1: Three dimensional problem

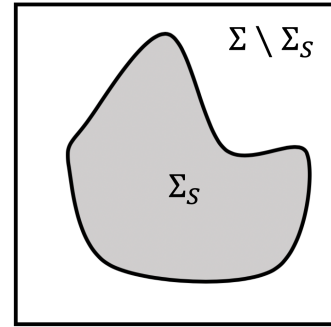


Figure 2: Working domain Σ composed of Σ_S and $\Sigma \setminus \Sigma_S$

2.2 Optimization problem

The working domain Σ is split into two different zones: the domain Σ_S must be built during the scanning and the domain $\Sigma \setminus \Sigma_S$ must remain powder (Figure 2). Controlling the building through the path is monitored by three different constraints that should vanish [9, 10].

- Control of the solid region. The part $\Sigma_S \subset \Sigma$ must melt before solidification. Thus $\forall x \in \Sigma_S$, there must be a time $t \in (0, t_F)$ such that the temperature $y(t, x)$ is above the phase change (fusion) temperature y_ϕ , namely $y(t, x) \geq y_\phi$ (the change of phase is in this model assumed to be instantaneous which is of course an approximation). Therefore, the following constraint, with the notation $(\cdot)^+ = \max(0, \cdot)$,

$$C_\phi(\Gamma, y) = \int_{\Sigma_S} \left[\left(y_\phi - \max_{t \in (0, t_F)} y(t, x) \right)^+ \right]^2 dx,$$

has to vanish to ensure that the desired solid region is built with a given path Γ . In the following, we need to differentiate this function with respect to t_F and y . Since the maximum function is not differentiable, it is approximated by a L^p -norm. The effective or approximate version of the constraint is given by:

$$C_\phi(\Gamma, y) = \int_{\Sigma_S} \left[(y_\phi - N_p(\Gamma, y)(x))^+ \right]^2 dx, \quad N_p(\Gamma, y)(x) = \left(\frac{1}{t_F} \int_0^{t_F} |y(t, x)|^p dt \right)^{1/p}$$

The integer p has a real impact on the constraint (accuracy and numerical computations issues). In numerical applications, this coefficient is fixed to $p = 64$.

- Control of the powder region. The part $\Sigma \setminus \Sigma_S$ must remain powder. Thus, at each point $x \in \Sigma \setminus \Sigma_S$, the temperature, $y(t, x)$, must remain under a maximum temperature $y_{\Sigma \setminus \Sigma_S} \leq y_\phi$, namely $y(t, x) \leq y_{\Sigma \setminus \Sigma_S}$. A constraint, referred to as "maximum temperature constraint out of the part" in the following, can then be introduced

$$C_{\Sigma \setminus \Sigma_S}(\Gamma, y) = \frac{1}{t_F} \int_{\Sigma \setminus \Sigma_S} \int_0^{t_F} \left[(y(t, x) - y_{\Sigma \setminus \Sigma_S})^+ \right]^2 dt dx.$$

- Control of the defects. To avoid the appearance of defects in the part during its building (especially residual stresses and deformations), the maximum temperature is required to stay below a fixed threshold. Thus, at each point $x \in \Sigma_S$, the temperature $y(t, x)$ must remain below a maximum temperature y_{Σ_S} , namely $y(t, x) \leq y_{\Sigma_S}$. The choice of the maximal temperature y_{Σ_S} is somehow arbitrary and obviously impacts the optimization results. For further details, the reader can refer to [9] and especially to Chapter 7. The "maximum temperature constraint in the part" is thus defined by

$$C_{\Sigma_S}(\Gamma, y) = \frac{1}{t_F} \int_{\Sigma_S} \int_0^{t_F} \left[(y(t, x) - y_{\Sigma_S})^+ \right]^2 dt dx.$$

The objective is to minimize the final time t_F under the temperature constraints $C_\phi = C_{\Sigma \setminus \Sigma_S} = C_{\Sigma_S} = 0$. This leads to the following optimization problem:

$$\min_{\Gamma} J(\Gamma) = t_F \quad \text{such that} \quad \begin{cases} C_\phi = C_{\Sigma_S} = C_{\Sigma \setminus \Sigma_S} = 0, \\ y \text{ solution of (1)}. \end{cases} \quad (3)$$

Remark 1. *The different constraints chosen for this model could be improved. The phase constraint C_ϕ is built as if the change of phase were instantaneous whereas in reality, the temperature must stand above the change of phase temperature for a small amount of time which could be modeled. Alternatively, the change of phase temperature y_ϕ could be chosen higher than the real one. The maximum temperature constraint in the part C_{Σ_S} is supposed to control the residual stresses. Of course, the resolution of a mechanical problem or the control of the maximum temperature spatial gradient would provide more information. Improving these two constraints is part of the perspectives.*

3 Discrete model and optimization algorithm

To optimize the path, a descent gradient method is used. To compute the corresponding descent direction, the optimization problem is first discretized, implying the choice of a working domain mesh and a path numerical representation. Then, a numerical gradient is found and finally an optimization algorithm is set.

3.1 Path representation and discrete model

To develop an iterative optimization algorithm adapting the source path, a numerical framework must be chosen, including a path representation and a mesh of the working domain Σ . We choose to maintain the working domain mesh fixed along the iterations and to represent the path as a broken line (in the spirit of front tracking methods, see [9, 47] for further details). Of course, other choices could be possible, like splines, as in [2, 3], which are smoother but somehow more complex to manipulate. The broken line path can be defined

through several variables. A first idea, developed in [9, 10], is derived from optimal control: most of the resolution techniques for problems mixing partial and ordinary differential equations [16, 32, 50, 51] choose the path curvature as control. In [9, 10], a path control based on the direction of each broken line segment has been experimented. However, the control of the final time remains a complicated issue.

In this work, the broken line is represented by its nodes: at each iteration, we consider the path as a sequence of N_u points $u = (u_i)_{i \in \llbracket 1, N_u \rrbracket}$. The heat equation is discretized with an implicit Euler scheme following these points with the time step defined by $\forall i \in \llbracket 1, N_u - 1 \rrbracket, \Delta t_i = |u_{i+1} - u_i|/V$ (and V fixed to 1 ms^{-1} in this section). These $(N_u - 1)$ time steps depend on the path but we need an additional initial time step Δt_0 to have as many of them as we have points u_i in the path. The time step Δt_0 is arbitrarily fixed. This time step can be seen as the required time for the source to be switched on. We set $y_0 = y_{\text{ini}}$. Then, $\forall i \in \llbracket 0, N_u - 1 \rrbracket$,

$$\begin{cases} \rho c_P \frac{y_{i+1} - y_i}{\Delta t_i} - \nabla (\lambda \nabla y_{i+1}) + \beta (y_{i+1} - y_{\text{ini}}) = P \exp\left(-\frac{|x - u_{i+1}|^2}{r^2}\right) & x \in \Sigma, \\ \lambda \partial_n y_{i+1} = 0 & x \in \partial \Sigma. \end{cases} \quad (4)$$

The final time is given by:

$$t_F = \sum_{i=0}^{N_u-1} \Delta t_i.$$

Because Δt_0 is arbitrarily fixed and not subject to optimization, it is removed from the final time sum in the following. The constraints are discretized through an implicit scheme corresponding to the heat equation's:

$$C_\phi = \int_{\Sigma_S} \left[(y_\phi - N_p)^+ \right]^2 dx = \int_{\Sigma_S} \left[\left(y_\phi - \left(\frac{1}{t_F} \sum_{i=0}^{N_u-1} \Delta t_i y_{i+1}^p \right)^{1/p} \right)^+ \right]^2 dx.$$

and

$$\begin{cases} C_{\Sigma_S} = \frac{1}{t_F} \int_{\Sigma_S} \sum_{i=0}^{N_u-1} \Delta t_i [(y_{i+1} - y_{\Sigma_S})^+]^2 dx, \\ C_{\Sigma \setminus \Sigma_S} = \frac{1}{t_F} \int_{\Sigma \setminus \Sigma_S} \sum_{i=0}^{N_u-1} \Delta t_i [(y_{i+1} - y_{\Sigma \setminus \Sigma_S})^+]^2 dx. \end{cases}$$

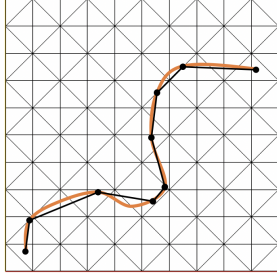


Figure 3: Front-tracking approach: fixed physical mesh and moving broken line path discretization

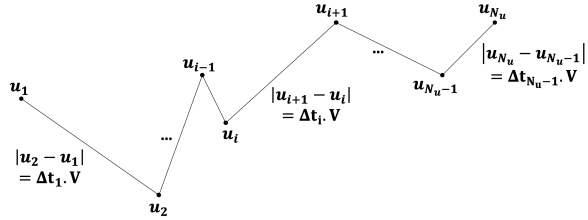


Figure 4: Path representation by a broken line

This path description requires running a specific step after each path modification in order to keep its representation correct. Indeed, at each iteration, each point of the sequence u is moved, modifying the distance between two consecutive points. In [10], a red discretization process has been described in the context of path discretization under a steady state assumption. The same process is chosen here, forcing the distance between two points to remain in a segment $[d_{\text{lower}}, d_{\text{upper}}]$. We choose in the following $2d_{\text{lower}} = d_{\text{upper}} = 1.4\Delta x$ where Δx is the typical mesh cell length. This arbitrary choice results from a compromise between accuracy of the description (related to the physical mesh accuracy) and computational time (note that the choice of these bounds impacts the optimal path, for further details on this topic, the interested reader is referred to [9]).

3.2 Differentiation of the discrete optimization problem with respect to the discrete path

Because the optimization method chosen is a gradient descent, the differentiation of each function with respect to the path is required. After discretization, this amounts to determining the derivative of each function with

respect to the nodal points defining the broken line.

To set the dependence of the steps Δt with respect to the points u , the definition of the discrete tangent vectors is recalled:

$$\forall i \in \llbracket 1, N_u - 1 \rrbracket, \tau_{\Gamma i} = \frac{(u_{i+1} - u_i)}{|u_{i+1} - u_i|}. \quad (5)$$

In the sequel the differential of a function $f(u)$ in the direction v is denoted by $Df(u)(v)$. Proposition 1 gives the derivative of each time step Δt_i ($i \in \llbracket 0, N_u - 1 \rrbracket$) with respect to the nodal points. It is recalled that Δt_0 is arbitrarily fixed and is thus independent from the points and V is fixed to 1 ms^1 .

Proposition 1. *Let $u = (u_i)_{i \in \llbracket 1, N_u \rrbracket} \in \Sigma^{N_u}$ the nodal points of the path Γ . Then, the time steps are differentiable with respect to u and, $\forall v \in \mathbb{R}^{N_u \times 2}$,*

$$\begin{cases} D\Delta t_i(u)(v) = \tau_{\Gamma i} \cdot (v_{i+1} - v_i) & \forall i \in \llbracket 1, N_u - 1 \rrbracket, \\ D\Delta t_0(u)(v) = 0 \end{cases}$$

Propositions 2, 3, 4 and 5 respectively give the derivative of the final time t_F , of the phase constraint C_ϕ , of the maximum temperature constraint out of the part $C_{\Sigma \setminus \Sigma_S}$ and of the maximum temperature constraint in the part C_{Σ_S} with respect to the nodal points. The complete proofs, which are standard from a mathematical point of view, can be found in [9], Chapter 7.

Proposition 2. *Let $u = (u_i)_{i \in \llbracket 1, N_u \rrbracket} \in \Sigma^{N_u}$ the nodal points of the path Γ . Then, the final time t_F is differentiable at u and, with $\tau_\Gamma \cdot v = \tau_{\Gamma x} v_x + \tau_{\Gamma y} v_y$, $\forall v \in \mathbb{R}^{N_u \times 2}$*

$$Dt_F(u)(v) = \tau_{\Gamma N_u - 1} \cdot v_{N_u} + \sum_{i=2}^{N_u-1} (\tau_{\Gamma i-1} - \tau_{\Gamma i}) \cdot v_i - \tau_{\Gamma 1} \cdot v_1,$$

To compute the derivative of the phase constraint C_ϕ , a sequence of adjoint functions $(p_i^\phi)_{i \in \llbracket 1, N_u \rrbracket} \in H^1(\Sigma)^{N_u}$ is defined by a backward in time system such that

$$\begin{cases} \rho c_P \frac{p_{N_u}^\phi}{\Delta t_{N_u-1}} - \nabla \cdot (\lambda \nabla p_{N_u}^\phi) + \beta p_{N_u}^\phi = \frac{2}{t_F} (y_\phi - N_p)^+ N_p^{1-p} y_{N_u}^{p-1} \mathbb{1}_{\Sigma_S} & \text{in } \Sigma \\ \lambda \partial_n p_{N_u}^\phi = 0 & \text{on } \partial \Sigma, \end{cases} \quad (6)$$

and $\forall i \in \llbracket 1, N_u - 1 \rrbracket$,

$$\begin{cases} \rho c_P \frac{p_i^\phi - p_{i+1}^\phi}{\Delta t_{i-1}} - \nabla \cdot (\lambda \nabla p_i^\phi) + \beta p_i^\phi = \frac{2}{t_F} (y_\phi - N_p)^+ N_p^{1-p} y_i^{p-1} \mathbb{1}_{\Sigma_S} & \text{in } \Sigma, \\ \lambda \partial_n p_i^\phi = 0 & \text{on } \partial \Sigma. \end{cases} \quad (7)$$

Proposition 3. *Let $u = (u_i)_{i \in \llbracket 1, N_u \rrbracket} \in \Sigma^{N_u}$ the nodal points of the path Γ . Then, the phase constraint C_ϕ is differentiable at u and, $\forall v \in \mathbb{R}^{N_u \times 2}$,*

$$\begin{aligned} DC_\phi(u)(v) = & \left[- \left(\text{HE}_2^\phi + C_2^\phi \right) \tau_{\Gamma 1} - \Delta t_0 \frac{2P}{r^2} \int_\Sigma p_1^\phi \exp \left(-\frac{|x - u_1|^2}{r^2} \right) (x - u_1) dx \right] \cdot v_1 \\ & + \sum_{i=2}^{N_u-1} \left[\left(\text{HE}_i^\phi + C_i^\phi \right) \tau_{\Gamma i-1} - \left(\text{HE}_{i+1}^\phi + C_{i+1}^\phi \right) \tau_{\Gamma i} - \Delta t_{i-1} \frac{2P}{r^2} \int_\Sigma p_i^\phi \exp \left(-\frac{|x - u_i|^2}{r^2} \right) (x - u_i) dx \right] \cdot v_i \\ & + \left[\left(\text{HE}_{N_u}^\phi + C_{N_u}^\phi \right) \tau_{\Gamma N_u-1} - \Delta t_{N_u-1} \frac{2P}{r^2} \int_\Sigma p_{N_u}^\phi \exp \left(-\frac{|x - u_{N_u}|^2}{r^2} \right) (x - u_{N_u}) dx \right] \cdot v_{N_u} \end{aligned}$$

with the adjoint $(p_i^\phi)_{i \in \llbracket 1, N_u \rrbracket} \in H^1(\Sigma)^{N_u}$ solution to (6) and (7) and $\forall i \in \llbracket 2, N_u \rrbracket$,

$$\begin{cases} \text{HE}_i^\phi = \int_\Sigma \left(\lambda \nabla y_i \cdot \nabla p_i^\phi + \beta (y_i - y_{ini}) p_i^\phi - P \exp \left(-\frac{(x - u_i)^2}{r^2} \right) p_i^\phi \right) dx, \\ C_i^\phi = \int_\Sigma \frac{2}{\rho t_F} (y_\phi - N_p)^+ \left[N_p - N_p^{1-p} y_i^p \right] \mathbb{1}_{\Sigma_S} dx. \end{cases}$$

To compute the derivative of the maximum temperature constraint out of the part $C_{\Sigma \setminus \Sigma_S}$, a sequence of adjoint functions $(p_i^{\Sigma \setminus \Sigma_S})_{i \in \llbracket 1, N_u \rrbracket} \in H^1(\Sigma)^{N_u}$ is defined by a backward system in time such that

$$\begin{cases} \rho_{CP} \frac{p_{N_u}^{\Sigma \setminus \Sigma_S}}{\Delta t_{N_u-1}} - \nabla \left(\lambda \nabla p_{N_u}^{\Sigma \setminus \Sigma_S} \right) + \beta p_{N_u}^{\Sigma \setminus \Sigma_S} = -\frac{2}{t_F} (y_{N_u} - y_{\Sigma \setminus \Sigma_S})^+ \mathbb{1}_{\Sigma \setminus \Sigma_S} & \text{in } \Sigma \\ \lambda \partial_n p_{N_u}^{\Sigma \setminus \Sigma_S} = 0 & \text{on } \partial \Sigma, \end{cases} \quad (8)$$

and $\forall i \in \llbracket 1, N_u - 1 \rrbracket$,

$$\begin{cases} \rho_{CP} \frac{p_i^{\Sigma \setminus \Sigma_S} - p_{i+1}^{\Sigma \setminus \Sigma_S}}{\Delta t_{i-1}} - \nabla \left(\lambda \nabla p_i^{\Sigma \setminus \Sigma_S} \right) + \beta p_i^{\Sigma \setminus \Sigma_S} - \frac{2}{t_F} (y_i - y_{\Sigma \setminus \Sigma_S})^+ \mathbb{1}_{\Sigma \setminus \Sigma_S} & \\ \text{in } \Sigma & \\ \lambda \partial_n p_i^{\Sigma \setminus \Sigma_S} = 0 & \\ \text{on } \partial \Sigma. & \end{cases} \quad (9)$$

Proposition 4. Let $u = (u_i)_{i \in \llbracket 1, N_u \rrbracket} \in \Sigma^{N_u}$ the nodal points of the path Γ . Then, the maximum temperature constraint out of the part $C_{\Sigma \setminus \Sigma_S}$ is differentiable at u and, $\forall v \in \mathbb{R}^{N_u \times 2}$,

$$\begin{aligned} DC_{\Sigma \setminus \Sigma_S}(u)(v) &= \left[- \left(\text{HE}_2^{\Sigma \setminus \Sigma_S} + C_2^{\Sigma \setminus \Sigma_S} \right) \tau_{\Gamma_1} - \Delta t_0 \frac{2P}{r^2} \int_{\Sigma} p_1^{\Sigma \setminus \Sigma_S} \exp \left(-\frac{|x - u_1|^2}{r^2} \right) (x - u_1) dx \right] \cdot v_1 \\ &+ \sum_{i=2}^{N_u-1} \left[\left(\text{HE}_{i+1}^{\Sigma \setminus \Sigma_S} + C_{i+1}^{\Sigma \setminus \Sigma_S} \right) \tau_{\Gamma_{i-1}} - \left(\text{HE}_i^{\Sigma \setminus \Sigma_S} + C_i^{\Sigma \setminus \Sigma_S} \right) \tau_{\Gamma_i} - \Delta t_{i-1} \frac{2P}{r^2} \int_{\Sigma} p_i^{\Sigma \setminus \Sigma_S} \exp \left(-\frac{|x - u_i|^2}{r^2} \right) (x - u_i) dx \right] \cdot v_i \\ &+ \left[\left(\text{HE}_{N_u}^{\Sigma \setminus \Sigma_S} + C_{N_u}^{\Sigma \setminus \Sigma_S} \right) \tau_{\Gamma_{N_u-1}} - \Delta t_{N_u-1} \frac{2P}{r^2} \int_{\Sigma} p_{N_u}^{\Sigma \setminus \Sigma_S} \exp \left(-\frac{|x - u_{N_u}|^2}{r^2} \right) (x - u_{N_u}) dx \right] \cdot v_{N_u} \end{aligned}$$

with the adjoint $(p_i^{\Sigma \setminus \Sigma_S})_{i \in \llbracket 1, N_u \rrbracket} \in H^1(\Sigma)^{N_u}$ solution to (8) and (9) and $\forall i \in \llbracket 2, N_u \rrbracket$,

$$\begin{cases} \text{HE}_i^{\Sigma \setminus \Sigma_S} = \int_{\Sigma} \left(\lambda \nabla y_i \cdot \nabla p_i^{\Sigma \setminus \Sigma_S} + \beta (y_i - y_{im_i}) p_i^{\Sigma \setminus \Sigma_S} - P \exp \left(-\frac{(x - u_i)^2}{r^2} \right) p_i^{\Sigma \setminus \Sigma_S} \right) dx, \\ C_i^{\Sigma \setminus \Sigma_S} = \frac{1}{t_F} \left[\int_{\Sigma} \left[(y_i - y_{\Sigma \setminus \Sigma_S})^+ \right]^2 \mathbb{1}_{\Sigma \setminus \Sigma_S} dx - C_{\Sigma \setminus \Sigma_S} \right] \end{cases}$$

To compute the derivative of the maximum temperature constraint out of the part C_{Σ_S} , a sequence of adjoint functions $(p_i^{\Sigma_S})_{i \in \llbracket 1, N_u \rrbracket} \in H^1(\Sigma)^{N_u}$ is defined by a backward system in time such that

$$\begin{cases} \rho_{CP} \frac{p_{N_u}^{\Sigma_S}}{\Delta t_{N_u-1}} - \nabla \left(\lambda \nabla p_{N_u}^{\Sigma_S} \right) + \beta p_{N_u}^{\Sigma_S} = -\frac{2}{t_F} (y_{N_u} - y_{\Sigma_S})^+ \mathbb{1}_{\Sigma_S} & \text{in } \Sigma \\ \lambda \partial_n p_{N_u}^{\Sigma_S} = 0 & \text{on } \partial \Sigma, \end{cases} \quad (10)$$

and $\forall i \in \llbracket 1, N_u - 1 \rrbracket$,

$$\begin{cases} \rho_{CP} \frac{p_i^{\Sigma_S} - p_{i+1}^{\Sigma_S}}{\Delta t_{i-1}} - \nabla \left(\lambda \nabla p_i^{\Sigma_S} \right) + \beta p_i^{\Sigma_S} = -\frac{2}{t_F} (y_i - y_{\Sigma_S})^+ \mathbb{1}_{\Sigma_S} & \text{in } \Sigma \\ \lambda \partial_n p_i^{\Sigma_S} = 0 & \text{on } \partial \Sigma. \end{cases} \quad (11)$$

Proposition 5. Let $u = (u_i)_{i \in \llbracket 1, N_u \rrbracket} \in \Sigma^{N_u}$ the nodal points of the path Γ . Then, the maximum temperature constraint in the part C_{Σ_S} is differentiable at u and, $\forall v \in \mathbb{R}^{N_u \times 2}$,

$$\begin{aligned} DC_{\Sigma_S}(u)(v) &= \left[- \left(\text{HE}_2^{\Sigma_S} + C_2^{\Sigma_S} \right) \tau_{\Gamma_1} - \Delta t_0 \frac{2P}{r^2} \int_{\Sigma} p_1^{\Sigma_S} \exp \left(-\frac{(x - u_1)^2}{r^2} \right) (x - u_1) dx \right] \cdot v_1 \\ &+ \sum_{i=2}^{N_u-1} \left[\left(\text{HE}_{i+1}^{\Sigma_S} + C_{i+1}^{\Sigma_S} \right) \tau_{\Gamma_{i-1}} - \left(\text{HE}_i^{\Sigma_S} + C_i^{\Sigma_S} \right) \tau_{\Gamma_i} - \Delta t_{i-1} \frac{2P}{r^2} \int_{\Sigma} p_i^{\Sigma_S} \exp \left(-\frac{(x - u_i)^2}{r^2} \right) (x - u_i) dx \right] \cdot v_i \\ &+ \left[\left(\text{HE}_{N_u}^{\Sigma_S} + C_{N_u}^{\Sigma_S} \right) \tau_{\Gamma_{N_u-1}} - \Delta t_{N_u-1} \frac{2P}{r^2} \int_{\Sigma} p_{N_u}^{\Sigma_S} \exp \left(-\frac{(x - u_{N_u})^2}{r^2} \right) (x - u_{N_u}) dx \right] \cdot v_{N_u} \end{aligned}$$

with the adjoint $(p_i^{\Sigma_S})_{i \in \llbracket 1, N_u \rrbracket} \in H^1(\Sigma)^{N_u}$ solution to (10) and (11) and $\forall i \in \llbracket 2, N_u \rrbracket$,

$$\begin{cases} \text{HE}_i^{\Sigma_S} = \int_{\Sigma} \lambda \nabla y_i \cdot \nabla p_i^{\Sigma_S} + \beta (y_i - y_{im_i}) p_i^{\Sigma_S} - P \exp \left(-\frac{(x - u_i)^2}{r^2} \right) p_i^{\Sigma_S} dx, \\ C_i^{\Sigma_S} = \frac{1}{t_F} \left[\int_{\Sigma} \left[(y_i - y_{\Sigma_S})^+ \right]^2 \mathbb{1}_{\Sigma_S} dx - C_{\Sigma_S} \right] \end{cases}$$

3.3 Transformation of the derivatives into gradients

The previous Propositions 2, 3, 4 and 5 have computed derivatives of various functions (t_F , C_ϕ , C_{Σ_S} , $C_{\Sigma \setminus \Sigma_S}$), which are generically denoted by $f(u)$, with respect to the points $u = (u_i)_{i \in [1, N_u]}$. The directional derivative can be written, for all $v \in \mathbb{R}^{N_u \times 2}$,

$$Df(u)(v) = \sum_{i=1}^{N_u} \Delta t_i G_i \cdot v_i,$$

for some collection of values $G_i \in \mathbb{R}^2$, $\forall i \in [1, N_u]$. This derivative $Df(u)$ of $f(u)$ must be transformed into a gradient $f'(u)$ which lies in the same space as u . A first obvious idea consists in choosing this gradient as $f'(u) \in \mathbb{R}^{N_u \times 2}$ such that $\forall i \in [1, N_u]$,

$$f'_i(u) = G_i.$$

This would indeed lead to $Df(u)(-f') = -\sum_{i=1}^{N_u} G_i^2$ making f' a descent direction.

There exist other possibilities to define gradients. Copying the strategy used in classical shape optimization [4, 12, 18, 39], a regularization process can be included into the transformation of the derivative into gradient: this process consists in practice to diffuse the derivative information at a node u_i to the neighbouring nodes and thus prevent the path to get too irregular. The gradient $f' \in \mathbb{R}^{N_u \times 2}$ is then defined as the solution to the discrete diffusion equation such that, $\forall v \in \mathbb{R}^{N_u \times 2}$,

$$\sum_{i=1}^{N_u-1} \Delta t_i \left[v_\Gamma^2 \left(\frac{f'_{i+1} - f'_i}{\Delta t_i} \right) \left(\frac{v_{i+1} - v_i}{\Delta t_i} \right) + \frac{f'_{i+1} v_{i+1} + f'_i v_i}{2} \right] = \sum_{i=1}^{N_u-1} \Delta t_i \frac{G_{i+1} v_{i+1} + G_i v_i}{2}. \quad (12)$$

The regularization coefficient v_Γ is arbitrarily fixed to $v_\Gamma = 20d_{\text{lower}}$. Note that, when f' is given by (12), the direction $-f'$ is a descent direction too. Further information on this regularization process as well as an analysis of the impact of this coefficient on the optimal path can be found in [9], Chapter 7.

Remark 2. Note that the formula given in (12) does not exactly correspond to a scalar product when $v_\Gamma \neq 0$. Yet, the direction $-f'$ is a descent direction and choosing $v_\Gamma = 0$ amounts to a L^2 -scalar product.

3.4 Optimization algorithm

Recall that the optimization problem (3) consists in minimizing the final time t_F while satisfying the temperature constraints $C_\phi = C_{\Sigma_S} = C_{\Sigma \setminus \Sigma_S} = 0$. The optimization variable in (3) is the path Γ . After discretization, the path is a broken line with nodal points u . Therefore, in the sequel the optimization variable is u instead of Γ . In order to deal with these constraints, an augmented Lagrangian method is chosen [41]. It consists in applying a classical Lagrangian method to a penalized function which amounts to solve, with μ_ϕ , μ_{Σ_S} , $\mu_{\Sigma \setminus \Sigma_S}$ fixed positive penalization coefficients,

$$\min_{u \in \Sigma^{N_u}} \max_{l_\phi \in \mathbb{R}, l_{\Sigma_S} \in \mathbb{R}, l_{\Sigma \setminus \Sigma_S} \in \mathbb{R}} \mathcal{L}_{\text{ALM}} \quad (13)$$

with

$$\mathcal{L}_{\text{ALM}} = t_F + l_\phi C_\phi + \frac{\mu_\phi}{2} C_\phi^2 + l_{\Sigma_S} C_{\Sigma_S} + \frac{\mu_{\Sigma_S}}{2} C_{\Sigma_S}^2 + l_{\Sigma \setminus \Sigma_S} C_{\Sigma \setminus \Sigma_S} + \frac{\mu_{\Sigma \setminus \Sigma_S}}{2} C_{\Sigma \setminus \Sigma_S}^2.$$

At each iteration, the update direction chosen is $d \in \mathbb{R}^{N_u \times 2}$ such that

$$d = - \left[t'_F(u) + (l_\phi + \mu_\phi C_\phi) C'_\phi(u) + (l_{\Sigma_S} + \mu_{\Sigma_S} C_{\Sigma_S}) C'_{\Sigma_S}(u) + (l_{\Sigma \setminus \Sigma_S} + \mu_{\Sigma \setminus \Sigma_S} C_{\Sigma \setminus \Sigma_S}) C'_{\Sigma \setminus \Sigma_S}(u) \right], \quad (14)$$

where t'_F , C'_ϕ , C'_{Σ_S} and $C'_{\Sigma \setminus \Sigma_S}$ are computed solving the regularization equation (12). Each point u_i is then moved along the direction d_i so that

$$u_i^{k+1} = u_i^k + s^k d_i^k. \quad (15)$$

The step is given as $s^k = \frac{C_s \Delta x}{\max_{i \in [1, N_u]} |d_i^k|}$. The coefficient C_s is initialized to 1 and updated depending on the success of the iteration, with the tolerance arbitrarily initialized to 2 and multiplied by 0.9 every 50 iterations:

$$\begin{cases} C_s^{k+1} = \max(1, 1.2C_s^k), & \text{if } \mathcal{L}_{\text{ALM}}^{k+1} \leq \text{tol} \mathcal{L}_{\text{ALM}}^k, \\ C_s^{k+1} = 0.6C_s^k, & \text{else.} \end{cases}$$

The update of the Lagrange multipliers follows

$$\begin{cases} l_\phi^{k+1} = l_\phi^k + \mu_\phi C_\phi^k, \\ l_{\Sigma_S}^{k+1} = l_{\Sigma_S}^k + \mu_{\Sigma_S} C_{\Sigma_S}^k, \\ l_{\Sigma \setminus \Sigma_S}^{k+1} = l_{\Sigma \setminus \Sigma_S}^k + \mu_{\Sigma \setminus \Sigma_S} C_{\Sigma \setminus \Sigma_S}^k. \end{cases} \quad (16)$$

In all numerical applications, the multipliers are initialized to 0 ($l_\phi^0 = l_{\Sigma_s}^0 = l_{\Sigma \setminus \Sigma_s}^0 = 0$) and the penalization coefficients are set to 10 ($\mu_\phi = \mu_{\Sigma_s} = \mu_{\Sigma \setminus \Sigma_s} = 10$). As for the number of iterations, it is bounded by 800. However, if the coefficient C_s gets smaller than 10^{-6} the algorithm is stopped. A recap of the optimization process is given in Algorithm 1.

```

1 mesh creation and initialization of the path;
2 rediscrctization of the path;
3 resolution of the heat equation and computation of the objective function and constraints;
4 computation of the derivatives and regularization to get the descent direction;
5 while iteration  $n \leq 800$  and  $C_s \geq 10^{-6}$  do
6   update of the tolerance;
7   line variation such that  $\Gamma^{n+1} = \Gamma^n + s^n d^n$ ;
8   rediscrctization of the path;
9   resolution of the heat equation, computation of the objective function and constraint;
10  if  $\mathcal{L}_{\text{ALM}}(\Gamma^{n+1}) < \mathcal{L}_{\text{ALM}}(\Gamma^n) * \text{tol}^n$  then
11    iteration accepted;
12    Lagrange multiplier updated;
13    step increased ;
14    update of the variables;
15    computation of the derivatives and regularization to get the descent direction;
16  end
17  else
18    iteration refused;
19    step decreased;
20  end
21 end

```

Algorithm 1: Optimization iterative algorithm.

Remark 3. *The temperature constraints are taken into account by an augmented Lagrangian method in our optimization algorithm. This method is simple, easy to code and to explain. However, it only ensures the fulfillment of the constraints at convergence which might not happen in a finite number of iterations. This choice explains, in the numerical applications, that the constraints are slightly above 0 at the final iteration. The model and optimization method proposed here could be used combined with other optimization algorithms or other augmented Lagrangian coefficients (see [9] for an analysis of this issue). For example, the approach proposed in [23] could be used and would probably lead to results better satisfying the constraints. This remains part of the perspectives.*

4 Numerical results

The working domain considered is $\Sigma = [-0.7, 0.7] \times [-0.7, 0.7]$ (given in *mm*) meshed with 12800 triangular elements. The accuracy of the discretized path is chosen such that $d_{\text{lower}} = 0.7\Delta x \leq \Delta u \leq 1.4\Delta x = d_{\text{upper}}$, with Δx the mean mesh element size, and the regularization coefficient as $\nu_\Gamma = 20d_{\text{lower}}$. The coefficient Δt_0 is fixed to d_{upper} . The finite element analysis is performed with Freefem 3.56 [28] and Python 3.6.0. The resolution of the different linear systems is done using a conjugate gradient method (library `scipy.sparse.linalg.cg` in Python, with a tolerance set to 10^{-10} for the convergence). The complete code is available on github (<https://gitlab.labos.polytechnique.fr/mathilde.boissier/path-unsteady.git>).

Two different materials are considered in the following: the aluminium and the titanium. The parameters involved in the heat equation for each case are summed up in Table 1. We recall that the characteristic length L as well as the coefficient β have been chosen according to a calibration of the model presented in Section 2 (see [9], Chapter 4 for further details). In both cases, the initial temperature is fixed to $y_{\text{ini}} = 773K$, the source absorption coefficient $A = 0.12$, the source radius $r = 5.0 * 10^{-5}m$ and the characteristic length $L = 5.85 * 10^{-5}m$.

Metal	ρ_{cp} $JK^{-1}m^{-3}$	λ $Wm^{-1}K^{-1}$	\bar{P} W	β $WK^{-1}m^{-3}$	y_ϕ (K) K	y_{Σ_S} (K) K	$y_{\Sigma \setminus \Sigma_S}$ (K) K
Aluminium	$2144 * 10^3$	130	400	$\frac{\lambda}{L * 1.17 * 10^{-4}}$	870	1670	870
Titanium	$3536 * 10^3$	15	300	$\frac{\lambda}{L * 1.17 * 10^{-4}}$	1900	3400	1800

Table 1: Numerical values chosen in the aluminium and titanium test cases.

In both cases, four different shapes are associated to the part to build Σ_S : a simple square included in the working domain Σ (Σ_S homothety with ratio 0.9 of the domain Σ) displayed by Figure 5(a), and three different "objects" (zero-hole, one-hole and three-holes) respectively shown by Figure 5(b),(c),(d).

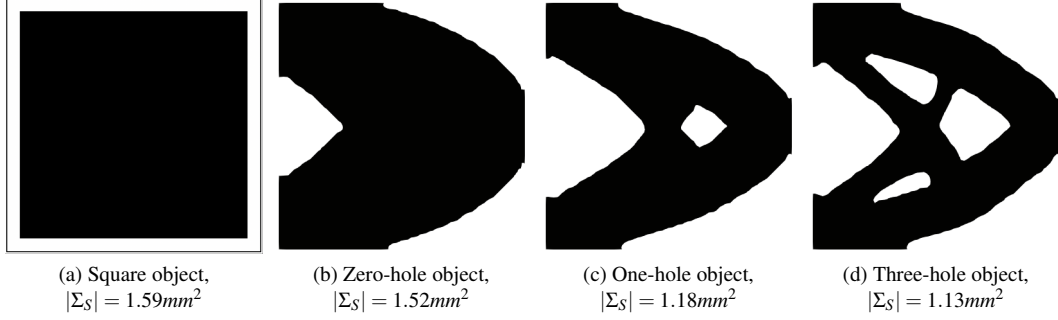


Figure 5: Different objects to build: the black area corresponds to Σ_S

For each optimization test, the numerical values are given adimensionalized ($|\Sigma| = 1.96mm^2$, $|\Sigma_S|$ given by Figure 5 and $|\Sigma \setminus \Sigma_S| = |\Sigma| - |\Sigma_S|$):

$$\bar{C}_\phi = \frac{C_\phi}{|\Sigma_S| y_\phi^2}, \quad \bar{C}_{\Sigma_S} = \frac{C_{\Sigma_S}}{|\Sigma_S| y_{\Sigma_S}^2}, \quad \bar{C}_{\Sigma \setminus \Sigma_S} = \frac{C_{\Sigma \setminus \Sigma_S}}{|\Sigma \setminus \Sigma_S| y_{\Sigma \setminus \Sigma_S}^2}. \quad (17)$$

4.1 Aluminium test case

The aluminium test case is first considered. To illustrate the optimization process, a first optimization is run starting from a zigzag with 6 lines. The path as well as the corresponding maximum temperature over the building at different iterations are given by Figure 6. The evolution of the final time t_F , the temperature constraints C_ϕ , C_{Σ_S} , $C_{\Sigma \setminus \Sigma_S}$ and the mean computational time per iteration is shown by Figure 7.

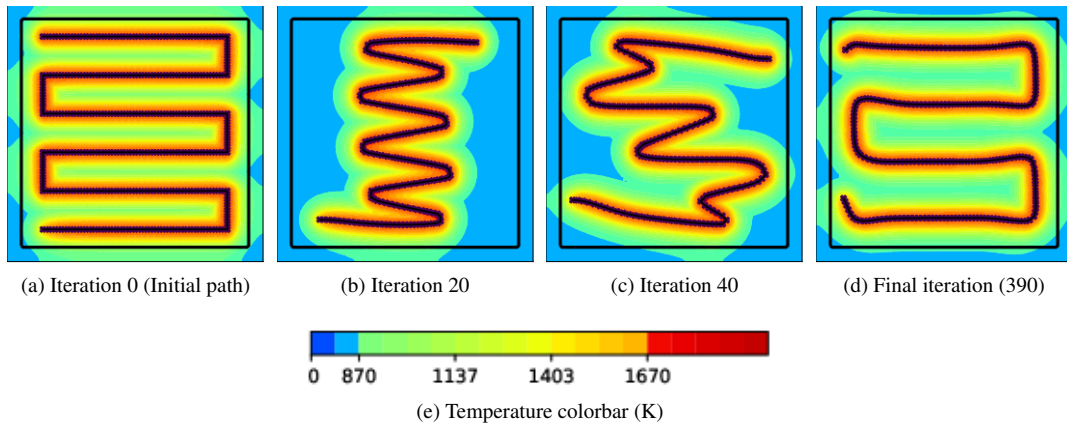


Figure 6: Path and maximum temperature ($\max_{t \in (0, t_F)} y(t)$) during the building with respect to the iterations, starting from a zigzag with 6 lines (aluminium)

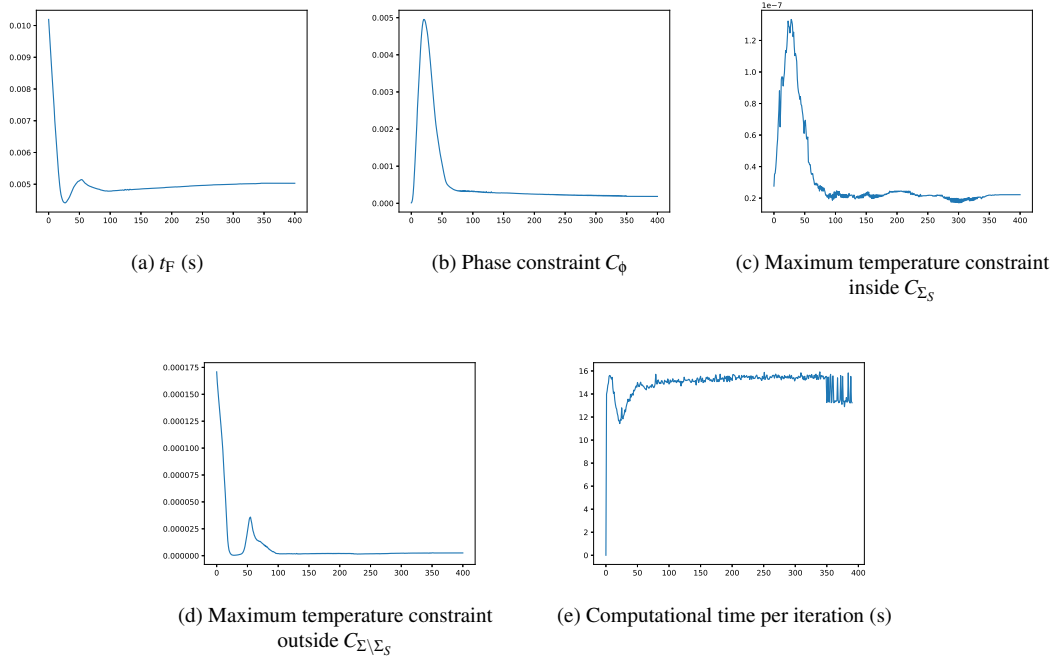


Figure 7: Evolution of the final time, the phase constraint, the maximum temperature constraints with respect to the iterations, starting from a zigzag with 6 lines (aluminium)

In this first test, the final time, i.e. the length of the path (the source velocity being constant), is first drastically reduced and then increased again, setting the new source points in accordance with the problem requirements. The decrease of the constraints can be observed and, if they end up slightly greater than 0, this is mainly because of the augmented Lagrangian method choice. As for the mean computational time, it is for most iterations around 8s. Note that the conjugate gradient method used in the point-based problem to solve linear problems could be accelerated by adding a preconditioner. This remains part of the perspectives.

The second test consists in starting from several different initializations to measure their impact on the final path. The initializations and results of the ten tests run are presented in Figure 8. Final adimensionalized values are summed up in Table 2. The graph of the final time with respect to the aggregated adimensionalized constraint $\bar{C} = \bar{C}_\phi + \bar{C}_{\Sigma_S} + \bar{C}_{\Sigma \setminus \Sigma_S}$ in each case is given in Figure 9.

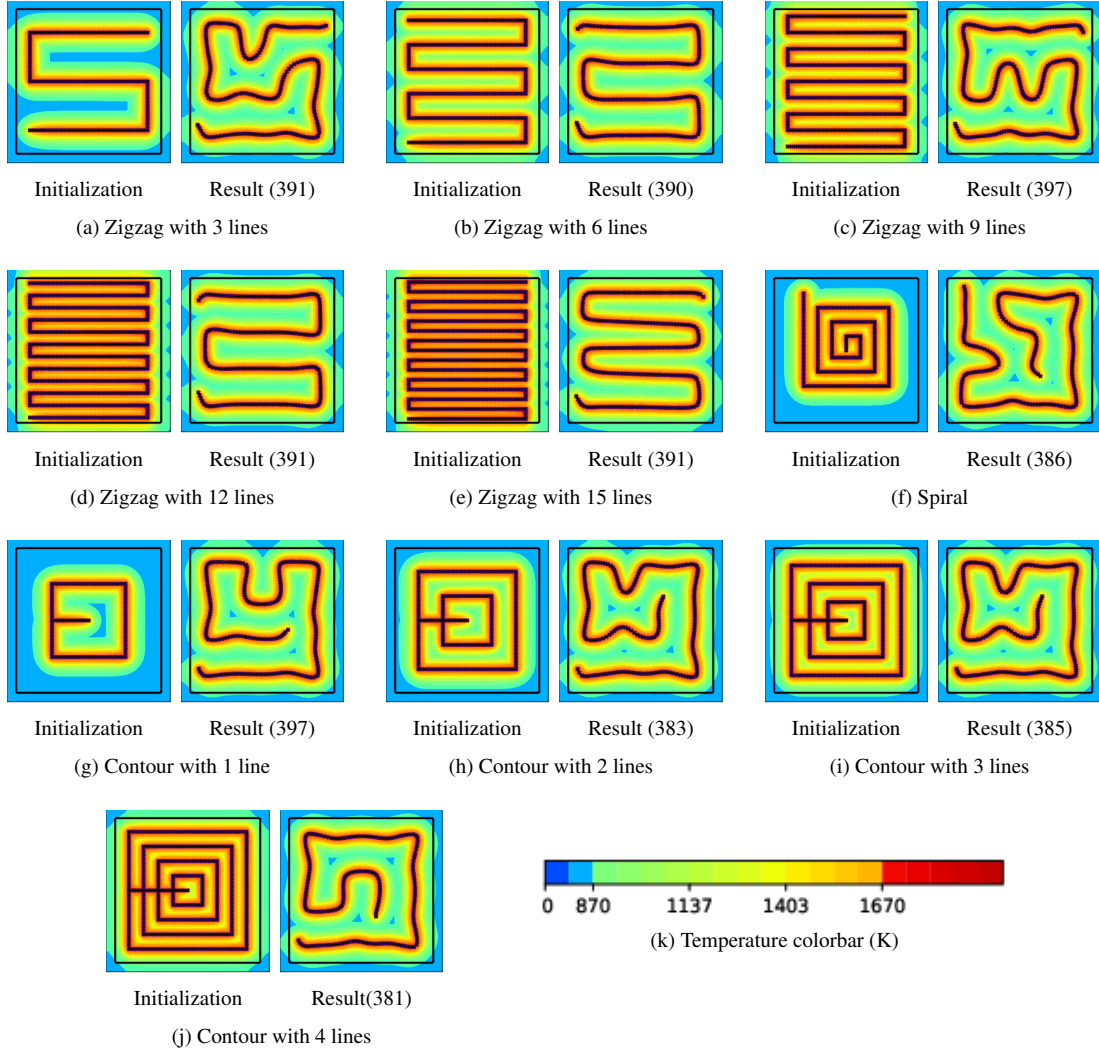


Figure 8: Path and maximum temperature ($\max_{t \in (0, t_F)} y(t)$) during the building depending on the initialization (aluminium)

Case	t_F^{fin} (s)	$\bar{C}_\phi^{\text{fin}}$	$\bar{C}_{\Sigma_S}^{\text{fin}}$	$\bar{C}_{\Sigma \setminus \Sigma_S}^{\text{fin}}$
zigzag 3 lines	$4.964e-03$	$1.72e-04$	$2.93e-09$	$1.00e-05$
zigzag 6 lines	$4.987e-03$	$1.32e-04$	$2.85e-09$	$1.34e-05$
zigzag 9 lines	$5.030e-03$	$1.54e-04$	$5.01e-09$	$9.11e-06$
zigzag 12 lines	$5.020e-03$	$1.16e-04$	$2.91e-09$	$1.49e-05$
zigzag 15 lines	$5.743e-03$	$1.16e-04$	$2.60e-09$	$2.23e-05$
spiral	$4.961e-03$	$1.75e-04$	$3.81e-09$	$5.13e-06$
contour 1 line	$4.983e-03$	$1.51e-04$	$3.70e-09$	$1.25e-05$
contour 2 lines	$4.925e-03$	$1.75e-04$	$4.44e-09$	$4.08e-06$
contour 3 lines	$4.930e-03$	$1.75e-04$	$4.27e-09$	$3.70e-06$
contour 4 lines	$4.849e-03$	$1.68e-04$	$3.12e-09$	$1.91e-06$

Table 2: Comparison of the final cost and constraints of the final results (aluminium)

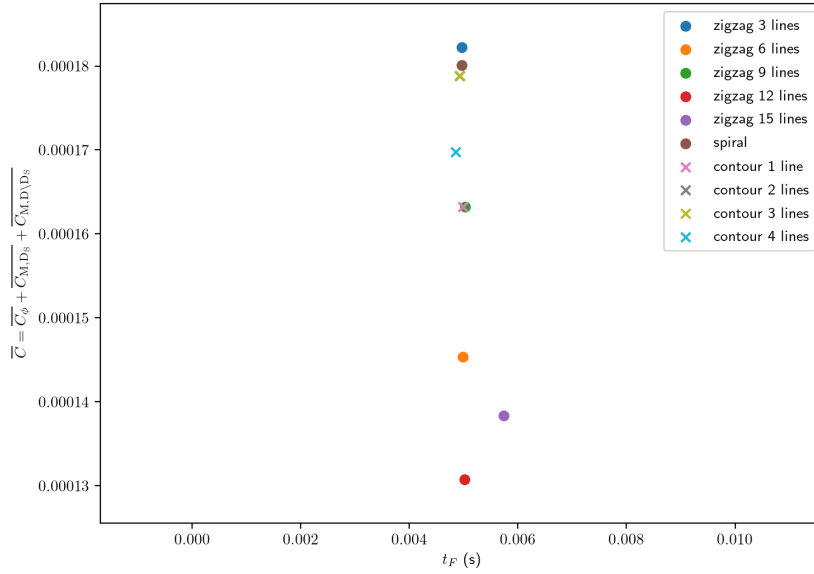


Figure 9: Constraint $\bar{C} = \bar{C}_\phi + \bar{C}_{\Sigma_S} + \bar{C}_{\Sigma \setminus \Sigma_S}$ with respect to the final time t_F (s) for the final results (aluminium)

The first conclusion to these different tests is that the algorithm is efficient. Indeed, but for the result coming out from the zigzag with 15 lines which final time is a little higher, each of the others appear intuitive and the final quantities are alike. In particular, the final time belongs mostly to $[4.9ms, 5.1ms]$, justifying the introduction of a notion of specific final time or energy (this notion has also been pointed out using a simplified steady model, see [9]). Moreover, the optimized path shapes form distinct clusters. Indeed, the contour with 2 and 3 lines lead to the same final path shape. A second cluster results from the 6-, 12- and 15-lines zigzag with a slight difference for the 15-line leading to a supplementary line. In addition, these last three cases are the most efficient with respect to the thermal constraints (see Figure 9).

In each of the cases, the phase constraint is not fully satisfied: for all the paths found, unmelted zones remain. This is proscribed by industrial applications which would rather increase the maximum temperature inside the part to build than leave powder unmelted. Thus the algorithm chosen should be modified to favor the phase constraint, modification requiring some care. Indeed, the phase constraint is only approximated and undervalued (see Section 2.2): it is already slightly favored. Unbalancing the different constraints could then result in large increases of the maximum temperature constraints. This algorithm modification could be dealt with by using another optimization algorithm than the Augmented Lagrangian method but this study remains part of the perspectives.

We finally focus on the building of three complicated geometries shown in Figure 5(b,c,d) (with respectively $|\Sigma_S^a| = 1.52mm^2$, $|\Sigma_S^b| = 1.18mm^2$ and $|\Sigma_S^c| = 1.13mm^2$). For each object, the optimization is run for two different initializations. The results for each object are presented by Figures 10, 11, 12, the graph shown in Figure 13 and Table 3.

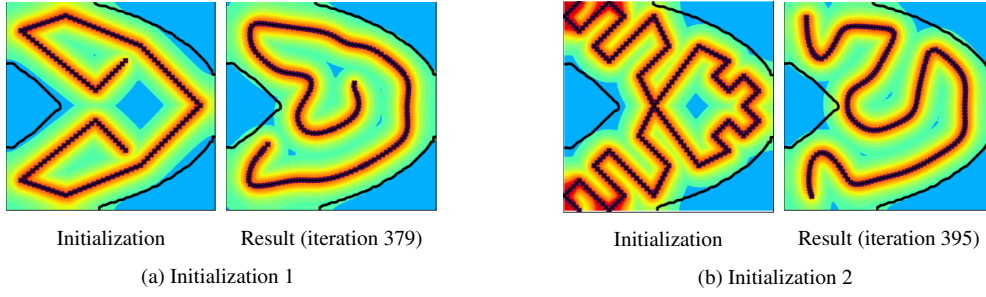


Figure 10: Path and maximum temperature ($\max_{t \in (0, t_F)} y(t)$) during the building depending on the initialization for the zero hole object (aluminium)

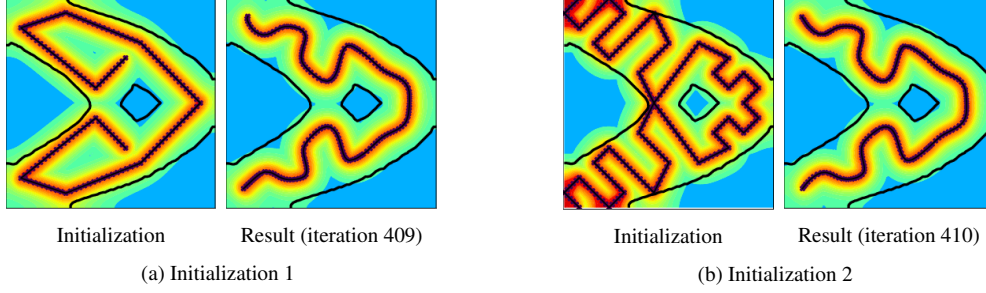


Figure 11: Path and maximum temperature ($\max_{t \in (0, t_F)} y(t)$) during the building depending on the initialization for the one hole object (aluminium)

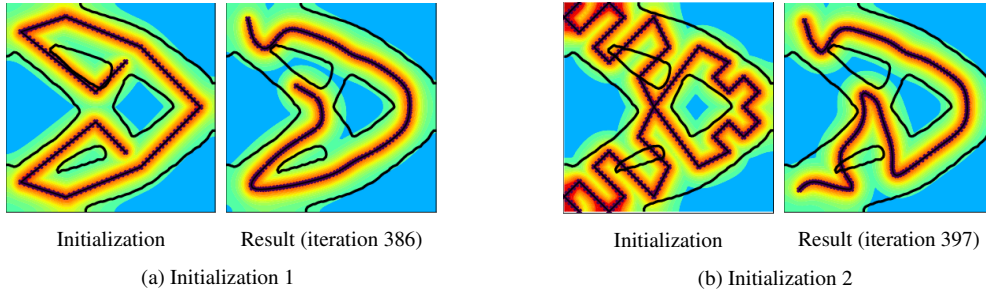
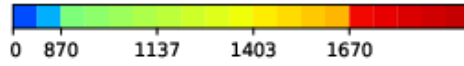


Figure 12: Path and maximum temperature ($\max_{t \in (0, t_F)} y(t)$) during the building depending on the initialization for the three holes object (aluminium)



Temperature colorbar

Case	t_F^{fin} (s)	$\bar{C}_\phi^{\text{fin}}$	$\bar{C}_{\Sigma_s}^{\text{fin}}$	$\bar{C}_{\Sigma \setminus \Sigma_s}^{\text{fin}}$
Zero hole				
initialization 1	$4.531e-03$	$1.46e-04$	$4.22e-09$	$2.39e-07$
initialization 2	$4.652e-03$	$1.68e-04$	$4.44e-09$	$1.31e-05$
One hole				
initialization 1	$3.532e-03$	$2.60e-04$	$7.71e-09$	$5.63e-07$
initialization 2	$3.499e-03$	$2.77e-04$	$7.59e-09$	$5.36e-07$
Three holes				
initialization 1	$3.710e-03$	$1.91e-04$	$6.67e-09$	$1.27e-04$
initialization 2	$3.900e-03$	$2.27e-04$	$1.50e-08$	$2.93e-04$

Table 3: Comparison of the final cost and constraints of the final results for the zero, one and three holes objects (aluminium)

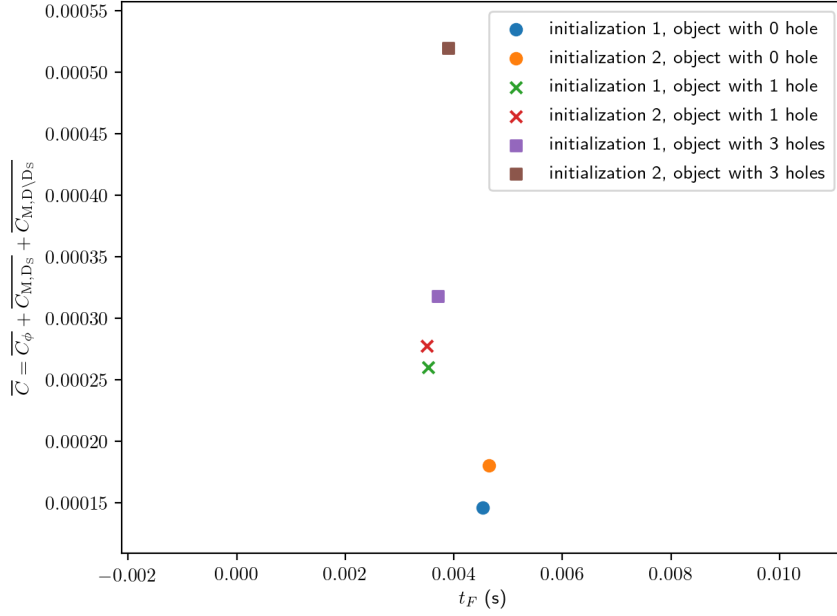


Figure 13: Constraint $\bar{C} = \bar{C}_\phi + \bar{C}_{\Sigma_S} + \bar{C}_{\Sigma_S \setminus \Sigma_S}$ with respect to the final time t_F (s) for the final results for the zero, one and three hole objects (aluminium)

The results from path optimization for a specific geometry confirm the previous remarks. First of all, at least for the two first objects, the algorithm leads to correct results and the final time values for the different initializations are similar. On the second object, the behavior of the algorithm is very satisfying, respecting the presence of the hole while showing a perfectly symmetrical and identical behavior for both initializations. As for the third object, the optimization is very hard: the aluminium conductivity is high and the shape appears very difficult to build while not melting the holes. This could be improved by better calibrating the model. Indeed, if leading to results that can be interpreted in a physical way, it remains not perfect and based on several assumptions. The developed method, yet requiring further work to accelerate the computations, could easily be adapted to a more complicated model. This remains part of perspectives.

4.2 Titanium test case

The titanium test case is then considered. As its conductivity is lower than that of aluminum, complications on the optimization process are expected. Indeed, a higher final time is required and, if this should increase the number of admissible solutions, this also increases the number of local minima. A first optimization is run starting from a zigzag with 12 lines. The path as well as the corresponding maximum temperature over the building at different iterations are given by Figure 14. The evolution of the final time t_F , the temperature constraints and the mean computational time per iteration is shown by Figure 15.

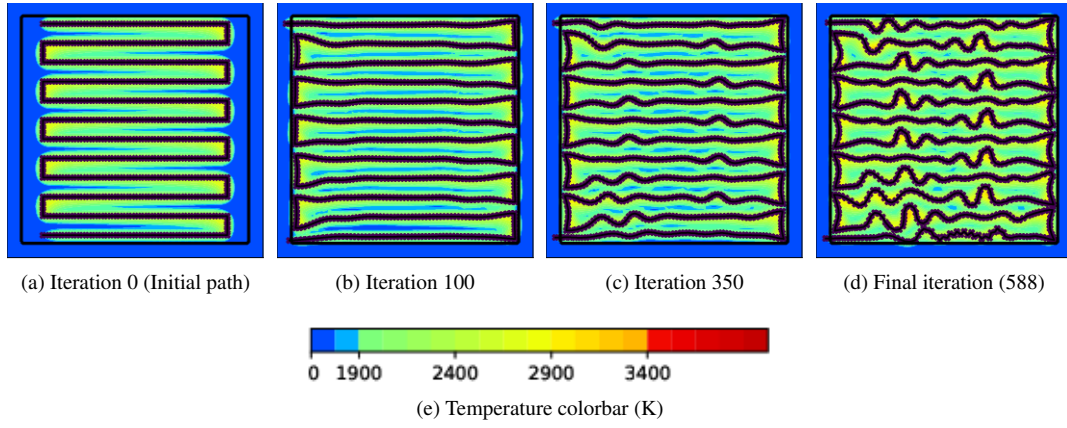


Figure 14: Path and maximum temperature ($\max_{t \in (0, t_F)} y(t)$) during the building with respect to the iterations, starting from a zigzag with 12 lines (titanium).

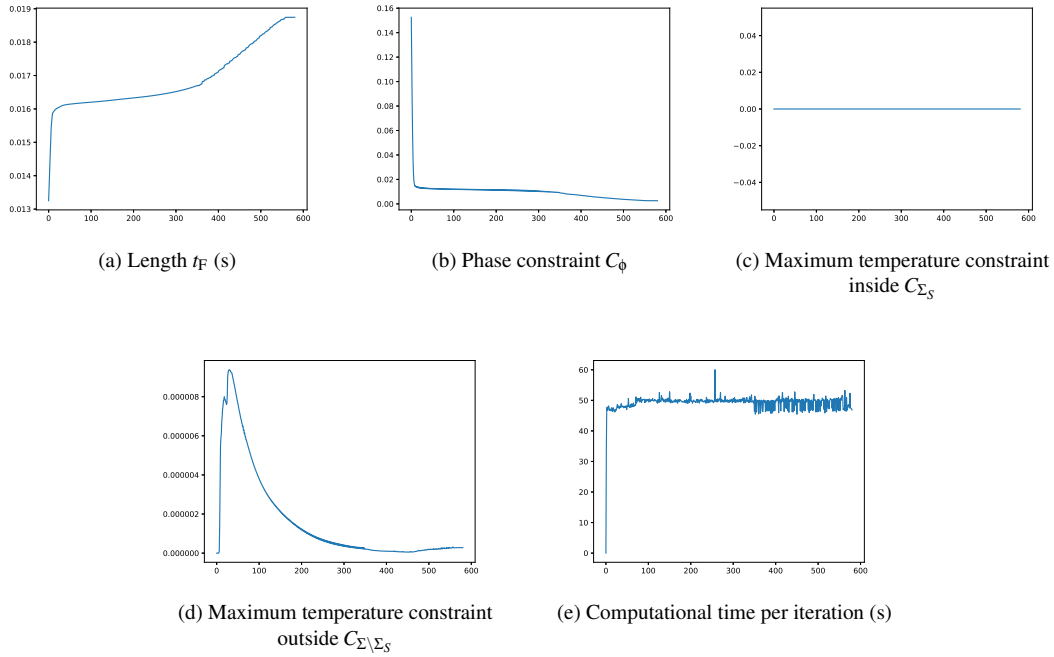


Figure 15: Evolution of the final time, the phase constraint, the maximum temperature constraints with respect to the iterations, starting from a zigzag with 12 lines (titanium).

The algorithm is able to lengthen the path (and thus the final time since the source velocity is constant) on the left and right sides (Figure 14(b)). Then, to remove the unmelted parts between the horizontal lines, perturbations are introduced to fill the holes (Figure 14(c)). These perturbations are deeply related with the regularization process (v_Γ in (3.3)). Note that the maximum temperature constraint is always satisfied : starting from this initialization, the maximum temperature should be chosen below 3400K to impact the final path.

Copying the tests run for the aluminium, several initializations are now tested. The initializations and results are presented in Figure 16. Final adimensionalized values are summed up in Table 4. The graph of the final time with respect to the aggregated adimensionalized constraint $\bar{C} = \bar{C}_\phi + \bar{C}_{\Sigma_S} + \bar{C}_{\Sigma \setminus \Sigma_S}$ in each case is given in Figure 17.

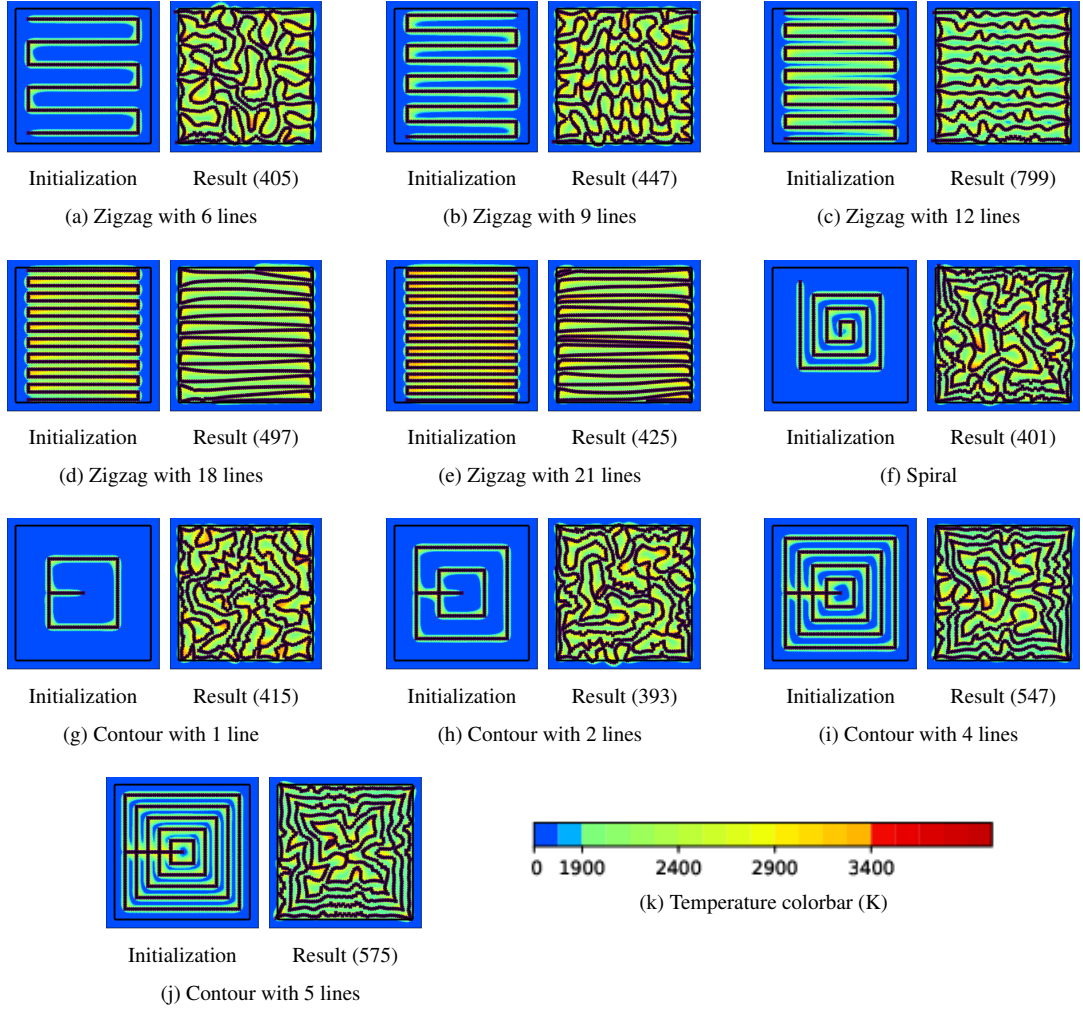


Figure 16: Path and maximum temperature ($\max_{t \in (0, t_F)} y(t)$) during the building depending on the initialization (titanium)

Case	t_F^{fin} (s)	$\bar{C}_\phi^{\text{fin}}$	$\bar{C}_{\Sigma_S}^{\text{fin}}$	$\bar{C}_{\Sigma \setminus \Sigma_S}^{\text{fin}}$
zigzag 6 lines	$2.243e-02$	$3.44e-07$	$0.00e+00$	$2.43e-05$
zigzag 9 lines	$2.307e-02$	$4.76e-07$	$0.00e+00$	$1.24e-05$
zigzag 12 lines	$1.874e-02$	$4.53e-04$	$0.00e+00$	$2.32e-07$
zigzag 18 lines	$2.246e-02$	$3.17e-06$	$0.00e+00$	$1.59e-05$
zigzag 21 lines	$2.496e-02$	$3.09e-06$	$0.00e+00$	$7.48e-06$
spiral	$2.386e-02$	$9.15e-06$	$0.00e+00$	$5.66e-06$
contour 1 line	$2.271e-02$	$1.79e-08$	$0.00e+00$	$6.99e-06$
contour 2 lines	$2.361e-02$	$1.20e-06$	$0.00e+00$	$1.83e-05$
contour 4 lines	$2.340e-02$	$1.01e-04$	$0.00e+00$	$4.68e-06$
contour 5 lines	$2.321e-02$	$1.32e-04$	$0.00e+00$	$5.19e-06$

Table 4: Comparison of the final cost and constraints of the final results (titanium)

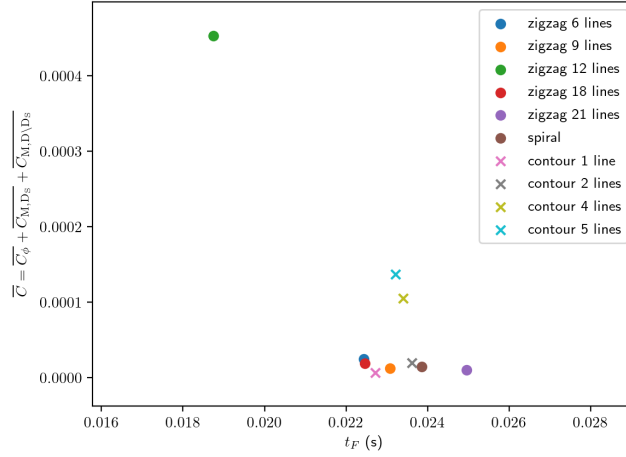


Figure 17: Constraint $\bar{C} = \bar{C}_\phi + \bar{C}_{\Sigma_S} + \bar{C}_{\Sigma \setminus \Sigma_S}$ with respect to the final time t_F (s) for the final results (titanium)

The results in the titanium test case are a lot more intricate than in the aluminium case, with many more local minima than with the aluminium. Yet, the optimization process works well with constraints satisfied and final times that get quite close to one another even if starting from very different initializations. Indeed, but for two of them, the final times all belong to $[22.4ms, 23.9ms]$. The two exceptions are for the zigzag with 21 lines and the zigzag with 12 lines. The first one has a very high initial final time and the algorithm does not manage to reduce enough the path length. The second initialization seems quite close to a good optimum and does not require much path modifications. The idea of specific energy is still valid when considering a material with lower conductivity.

In order to facilitate the optimization and obtain results that could be applied in the industry, the optimization should be run on smaller zones, thus reducing the number of local minima. We could then work on the expansion of these results for small domains to larger by concurrent optimization between several domains or symmetry conditions. These developments are part of the perspectives.

Finally, as for the aluminium, for each of the objects given in Figure 5, the optimization is run for two different initializations. The results for each object are presented by Figures 18, 19, 20, by the graph shown in Figure 21 and Table 5.

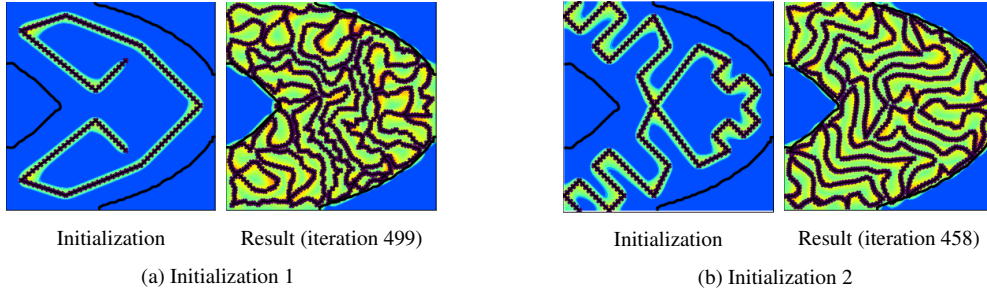


Figure 18: Path and maximum temperature ($\max_{t \in (0, t_F)} y(t)$) during the building depending on the initialization for the zero hole object (titanium)

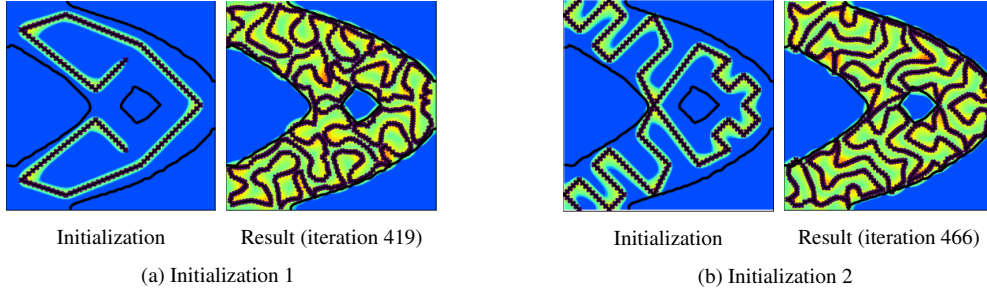


Figure 19: Path and maximum temperature ($\max_{t \in (0, t_F)} y(t)$) during the building depending on the initialization for the one hole object (titanium)

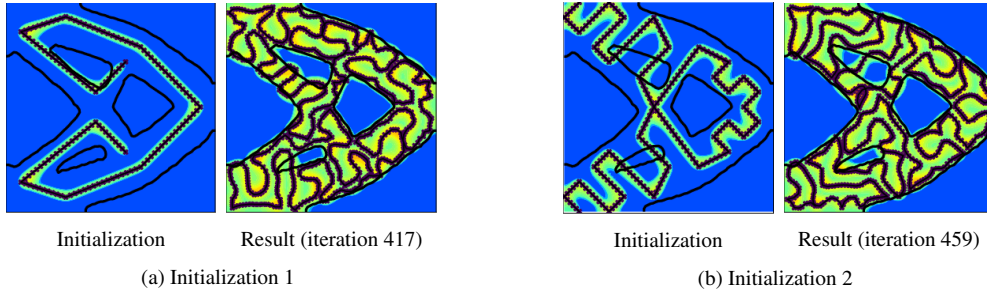
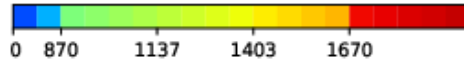


Figure 20: Path and maximum temperature ($\max_{t \in (0, t_F)} y(t)$) during the building depending on the initialization for the three holes object (titanium)



Temperature colobar

Case	t_F^{fin} (s)	$\overline{C}_\phi^{\text{fin}}$	$\overline{C}_{\Sigma_S}^{\text{fin}}$	$\overline{C}_{\Sigma \setminus \Sigma_S}^{\text{fin}}$
Zero hole				
initialization 1	$2.238e-02$	$1.80e-10$	$0.00e+00$	$2.03e-05$
initialization 2	$2.050e-02$	$2.72e-08$	$0.00e+00$	$1.30e-05$
One hole				
initialization 1	$1.643e-02$	$3.20e-09$	$0.00e+00$	$1.12e-05$
initialization 2	$1.564e-02$	$1.45e-07$	$0.00e+00$	$1.51e-05$
Three holes				
initialization 1	$1.640e-02$	$1.03e-08$	$0.00e+00$	$4.59e-05$
initialization 2	$1.547e-02$	$2.68e-07$	$0.00e+00$	$4.67e-05$

Table 5: Comparison of the final cost and constraints of the final results for the zero, one and three holes objects (titanium)

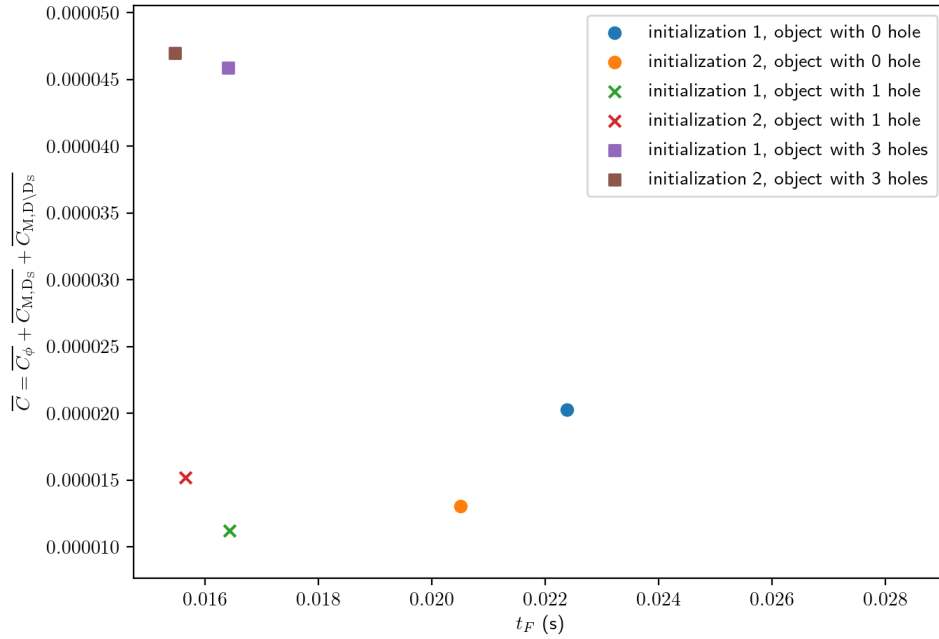


Figure 21: Constraint $\bar{C} = \bar{C}_\phi + \bar{C}_{\Sigma_S} + \bar{C}_{\Sigma \setminus \Sigma_S}$ with respect to the final time t_F (s) for the final results (titanium)

The results for each of the objects are better than for the aluminium. Indeed, the shape is better respected while keeping the maximum temperature constraint low. This conclusion was expected. Since the titanium's conduction is lower than the aluminium's, building thin bars is easier which explains the results obtained for the object with three holes. However, the final paths are once again too complicated to be directly applied in the industry: the curvature should be controlled and we could split the object to work on smaller domains thus reducing the number of local minima. These adaptations to further industrial requirements are part of the perspectives.

5 Conclusion and perspectives

We developed in this work a scanning path optimization algorithm controlling the residual stresses and taking into account the unsteady character of the travelling heat source. Although the resulting paths are intricate, especially for low conductivity materials, the optimization algorithm definitely proves its relevance since our results corroborate tendencies already mentioned in the literature. First of all, in accordance with the steady state case developed in [10], the results clearly depend on the initialization. Yet, whatever "correct" initialization is chosen, the scanning time and the constraints, for the optimized result, appear very similar: it hints towards the existence of a required energy related to the material conductivity, the source properties (and especially its power) and the part's shape and topology [9, 13, 14, 24]. This amount of energy could be a very useful tool in the scanning path choice. Then, in accordance with the steady state case [11], the part's shape and topology impact the path quality. In particular, the shape thickness is involved into the path feasibility. These promising results point out several perspectives in order to better understand how path and part's shape and topology are related. The optimization algorithm could be modified to better control the fulfillment of the constraints, for example replacing the Augmented Lagrangian method by a null space gradient algorithm, as developed in [23]. The path description could be made more complex: in particular, kinematics could be taken into account. Indeed, in this work, the source velocity is assumed constant. However, it is not in practice and it is very much path-dependent (the velocity especially depends on the path curvature): including a velocity model (see [21] for example) would probably highly impact the optimal path. In a second phase, it would be very interesting to allow the source to be switched on and off along the building. Finally, the residual stresses control should be made more realistic by including a mechanical performance evaluation in the optimization.

6 Acknowledgments

This work is supported by the SOFIA project, funded by Bpifrance (Banque Publique d'Investissement). We thank Forian Feppon for providing some of his optimization routines.

References

- [1] A. AHRARI, K. DEB, S. MOHANTY, AND J. HATTEL, *Multi-objective optimization of cellular scanning strategy in selective laser melting*, in 2017 IEEE Congress on Evolutionary Computation (CEC), IEEE, 2017, pp. 2730–2737.
- [2] T. ALAM, *Some optimal control problem of partial differential equations and applications to the selective laser melting process (SLM)*, PhD thesis, Université Polytechnique Hauts-de-France, INSA Hauts-De-France, 2020.
- [3] T. ALAM, S. NICAISE, AND L. PAQUET, *An optimal control problem governed by the heat equation with nonconvex constraints applied to the selective laser melting process*, *Minimax Theory and its Applications*, 6 (2021).
- [4] G. ALLAIRE, C. DAPOGNY, AND F. JOUVE, *Shape and topology optimization*, vol. 22 of in *Geometric partial differential equations, Part II*, A. Bonito and R. Nochetto eds., pp.1-132, *Handbook of Numerical Analysis*, vol. 22, Elsevier, 2021.
- [5] G. ALLAIRE AND L. JAKABČIN, *Taking into account thermal residual stresses in topology optimization of structures built by additive manufacturing*, *Math. Models Methods Appl. Sci.*, 28 (2018), pp. 2313–2366.
- [6] E. ARKIN, M. HELD, AND C. SMITH, *Optimization problems related to zigzag pocket machining*, *Algorithmica*, 26 (2000), pp. 197–236.
- [7] V. BHAVAR, P. KATTIRE, V. PATIL, S. KHOT, K. GUJAR, AND R. SINGH, *A review on powder bed fusion technology of metal additive manufacturing*, in *Additive Manufacturing Handbook*, CRC Press, 2017, pp. 251–253.
- [8] M. BIHR, *Coupled topology optimisation of part and support for metal additive manufacturing*, PhD thesis, Ecole Polytechnique, to appear in 2021.
- [9] M. BOISSIER, *Coupling structural optimization and trajectory optimization methods in additive manufacturing*, PhD thesis, Institut Polytechnique de Paris, 2020.
- [10] M. BOISSIER, G. ALLAIRE, AND C. TOURNIER, *Additive manufacturing scanning paths optimization using shape optimization tools*, *Structural and Multidisciplinary Optimization*, 61 (2020), pp. 2437–2466.
- [11] ———, *Concurrent additive manufacturing shape optimization of the part and scanning path for additive manufacturing*, submitted, preprint hal-03124075, (2021).
- [12] M. BURGER, *A framework for the construction of level set methods for shape optimization and reconstruction*, *Interfaces Free Bound.*, 5 (2003), pp. 301–329.
- [13] F. CAIAZZO, V. ALFIERI, AND G. CASALINO, *On the relevance of volumetric energy density in the investigation of inconel 718 laser powder bed fusion*, *Materials*, 13 (2020), p. 538.
- [14] C. CEPEDA-JIMÉNEZ, F. POTENZA, E. MAGALINI, V. LUCHIN, A. MOLINARI, AND M. PÉREZ-PRADO, *Effect of energy density on the microstructure and texture evolution of ti-6al-4v manufactured by laser powder bed fusion*, *Materials Characterization*, (2020), p. 110238.
- [15] Q. CHEN, J. LIU, X. LIANG, AND A. TO, *A level-set based continuous scanning path optimization method for reducing residual stress and deformation in metal additive manufacturing*, *Computer Methods in Applied Mechanics and Engineering*, 360 (2020), p. 112719.
- [16] K. CHUDEJ, H. PESCH, M. WÄCHTER, G. SACHS, AND F. LE BRAS, *Stationary heat-constrained trajectory optimization of a hypersonic space vehicle by ODE-PDE-constrained optimal control*, in *Variational analysis and aerospace engineering*, vol. 33 of *Springer Optim. Appl.*, Springer, New York, 2009, pp. 127–144.

- [17] K. DAI AND L. SHAW, *Distortion minimization of laser-processed components through control of laser scanning patterns*, Rapid Prototyping Journal, 8 (2002), pp. 270–276.
- [18] F. DE GOURNAY, *Velocity extension for the level-set method and multiple eigenvalues in shape optimization*, SIAM J. Control Optim., 45 (2006), pp. 343–367.
- [19] T. DEBROY, H. WEI, J. ZUBACK, T. MUKHERJEE, J. ELMER, J. MILEWSKI, A. BEESE, A. WILSON-HEID, A. DE, AND W. ZHANG, *Additive manufacturing of metallic components—process, structure and properties*, Progress in Materials Science, 92 (2018), pp. 112–224.
- [20] D. DING, Z. PAN, D. CUIURI, H. LI, AND S. VAN DUIN, *Advanced design for additive manufacturing: 3d slicing and 2d path planning*, New trends in 3d printing, (2016), pp. 1–23.
- [21] T. DUONG, N. FERRIER, S. LAVERNHE, AND C. TOURNIER, *A kinematic simulation software for additive manufacturing metal deposition processes*, in ICWAM’19, International Congress On Welding, Additive Manufacturing And Associated Non Destructive Testing, 2019.
- [22] K. ETTAIEB, S. LAVERNHE, AND C. TOURNIER, *A flash-based thermal simulation of scanning paths in lpbfd additive manufacturing*, ahead-of-print (2021).
- [23] F. FEPPON, G. ALLAIRE, AND C. DAPOGNY, *Null space gradient flows for constrained optimization with applications to shape optimization*, ESAIM:COCV, 26 (2020), p. 90.
- [24] P. FERRO, R. MENEGHELLO, G. SAVIO, AND F. BERTO, *A modified volumetric energy density–based approach for porosity assessment in additive manufacturing process design*, The International Journal of Advanced Manufacturing Technology, (2020), pp. 1–11.
- [25] M. FRANCOIS, A. SUN, W. KING, N. HENSON, D. TOURET, C. BRONKHORST, N. CARLSON, C. NEWMAN, T. HAUT, J. BAKOSI, ET AL., *Modeling of additive manufacturing processes for metals: Challenges and opportunities*, Current Opinion in Solid State and Materials Science, 21 (2017).
- [26] W. GAO, Y. ZHANG, D. RAMANUJAN, K. RAMANI, Y. CHEN, C. WILLIAMS, C. WANG, Y. SHIN, S. ZHANG, AND P. ZAVATTIERI, *The status, challenges, and future of additive manufacturing in engineering*, Computer-Aided Design, 69 (2015), pp. 65–89.
- [27] K. GODINEAU, S. LAVERNHE, AND C. TOURNIER, *Calibration of galvanometric scan heads for additive manufacturing with machine assembly defects consideration*, Additive Manufacturing, 26 (2019), pp. 250–257.
- [28] F. HECHT, *New development in FreeFem++*, J. Numer. Math., 20 (2012), pp. 251–265.
- [29] D. HERZOG, V. SEYDA, E. WYCISK, AND C. EMMELMANN, *Additive manufacturing of metals*, Acta Materialia, 117 (2016), pp. 371–392.
- [30] J. JHABVALA, E. BOILLAT, T. ANTIGNAC, AND R. GLARDON, *On the effect of scanning strategies in the selective laser melting process*, Virtual and physical prototyping, 5 (2010), pp. 99–109.
- [31] H. JIA, H. SUN, H. WANG, Y. WU, AND H. WANG, *Scanning strategy in selective laser melting (slm): a review*, The International Journal of Advanced Manufacturing Technology, 113 (2021), pp. 2413–2435.
- [32] S.-J. KIMMERLE, M. GERDTS, AND R. HERZOG, *Optimal control of an elastic crane-trolley-load system—a case study for optimal control of coupled ODE-PDE systems*, Math. Comput. Model. Dyn. Syst., 24 (2018), pp. 182–206.
- [33] H. LI, Z. DONG, AND G. VICKERS, *Optimal toolpath pattern identification for single island, sculptured part rough machining using fuzzy pattern analysis*, Computer-Aided Design, 26 (1994), pp. 787–795.
- [34] J. LIU AND A. TO, *Deposition path planning-integrated structural topology optimization for 3d additive manufacturing subject to self-support constraint*, Computer-Aided Design, 91 (2017), pp. 27–45.
- [35] L. MA AND H. BIN, *Temperature and stress analysis and simulation in fractal scanning-based laser sintering*, The International Journal of Advanced Manufacturing Technology, 34 (2007), pp. 898–903.
- [36] M. MEGAHEB, H.-W. MINDT, N. N’DRI, H. DUAN, AND O. DESMAISON, *Metal additive-manufacturing process and residual stress modeling*, Integrating Materials and Manufacturing Innovation, 5 (2016), pp. 61–93.

- [37] P. MERCELIS AND J.-P. KRUTH, *Residual stresses in selective laser sintering and selective laser melting*, Rapid prototyping journal, 12 (2006), pp. 254–265.
- [38] J. MILEWSKI, *Additive manufacturing of metals*, From Fundamental Technology to Rocket Nozzles, Medical Implants, and Custom Jewelry, (2017), pp. 134–157.
- [39] B. MOHAMMADI AND O. PIRONNEAU, *Applied shape optimization for fluids*, Oxford university press, 2010.
- [40] S. MOHANTY AND J. HATTEL, *Reducing residual stresses and deformations in selective laser melting through multi-level multi-scale optimization of cellular scanning strategy*, in Laser 3D Manufacturing III, vol. 9738, International Society for Optics and Photonics, 2016.
- [41] J. NOCEDAL AND S. WRIGHT, *Numerical optimization*, Springer Series in Operations Research and Financial Engineering, Springer, New York, second ed., 2006.
- [42] J. OLIVEIRA, A. LALONDE, AND J. MA, *Processing parameters in laser powder bed fusion metal additive manufacturing*, Materials & Design, (2020), p. 108762.
- [43] V. RAJAN, V. SRINIVASAN, AND K. TARABANIS, *The optimal zigzag direction for filling a two-dimensional region*, Rapid Prototyping Journal, 7 (2001), pp. 231–241.
- [44] F. RASOANARIVO, P. RODRIGUEZ-AYCRBE, AND D. DUMUR, *Galvanometer scanner modeling for selective laser melting deflection system simulation*, in 2018 15th International Conference on Control, Automation, Robotics and Vision (ICARCV), IEEE, 2018, pp. 1170–1175.
- [45] H. SHIPLEY, D. MCDONNELL, M. CULLETON, R. COULL, R. LUPOI, G. O’DONNELL, AND D. TRIMBLE, *Optimisation of process parameters to address fundamental challenges during selective laser melting of ti-6al-4v: A review*, International Journal of Machine Tools and Manufacture, 128 (2018), pp. 1–20.
- [46] M. THOMPSON, G. MORONI, T. VANEKER, G. FADEL, R. CAMPBELL, I. GIBSON, A. BERNARD, J. SCHULZ, P. GRAF, B. AHUJA, ET AL., *Design for additive manufacturing: Trends, opportunities, considerations, and constraints*, CIRP annals, 65 (2016), pp. 737–760.
- [47] G. TRYGGVASON, B. BUNNER, A. ESMAEELI, D. JURIC, N. AL-RAWAHI, W. TAUBER, J. HAN, S. NAS, AND Y.-J. JAN, *A front-tracking method for the computations of multiphase flow*, Journal of computational physics, 169 (2001), pp. 708–759.
- [48] L. VAN BELLE, *Analyse, modélisation et simulation de l’apparition de contraintes en fusion laser métallique*, PhD thesis, INSA Lyon, 2013.
- [49] L. VAN BELLE, G. VANSTEENKISTE, AND J.-C. BOYER, *Investigation of residual stresses induced during the selective laser melting process*, in Key Engineering Materials, vol. 554, Trans Tech Publ, 2013, pp. 1828–1834.
- [50] S. WENDL, *On a prototype of an optimal control problem governed by ordinary and partial differential equations*, PhD thesis, University of Bayreuth, Faculty of Mathematics, Physics and Computer Sciences, 2014.
- [51] S. WENDL, H. PESCH, AND A. RUND, *On a state-constrained pde optimal control problem arising from ode-pde optimal control*, in Recent Advances in Optimization and its Applications in Engineering, Springer, 2010, pp. 429–438.